Nanoscale Advances

ROYAL SOCIETY OF CHEMISTRY

PAPER

View Article Online
View Journal | View Issue

Cite this: *Nanoscale Adv.*, 2021, **3**, 2887

Enhanced electrochemical activities of morphologically tuned $MnFe_2O_4$ nanoneedles and nanoparticles integrated on reduced graphene oxide for highly efficient supercapacitor electrodes†

R. Rajalakshmi, K. P. Remya, C. Viswanathan and N. Ponpandian *

The morphology of a nanoparticle strongly controls the path of electronic interaction, which directly correlates with the physicochemical properties and also the electrochemical comportment. Combining it with a two-dimensional (2D) material for a layer-by-layer approach will increase its possibilities in applications such as energy conversion and storage. Here, two different morphologies of $MnFe_2O_4$, nanoparticles and nanoneedles, are developed by a facile hydrothermal approach and sandwiched with reduced graphene oxide for constructing a 2D/3D sandwiched architecture. The rGO planar structure with abundant hierarchical short pores facilitates the thorough utilization of the utmost surface area to permeate the electrolyte within the structure to minimize the accumulation of rGO nanosheets laterally. The ferrite composited with rGO manifests high specific capacitance as the EDLC behaviour surpasses the faradaic pseudocapacitance boosting electrical conductivity compared to the as-synthesized $MnFe_2O_4$ structures. Benefiting from a 3D structure and the synergetic contribution of the $MnFe_2O_4$ nanoneedles and electrically conductive rGO layer, the $MnFe_2O_4$ nanoneedles@rGO electrode exhibits a high areal capacitance of 890 mF cm^{-2} and a remarkable specific capacitance of 1327 F g^{-1} at a current density of 5 mA cm^{-2}. 93.36% of the initial capacitance was retained after 5000 cycles in 1 mol L^{-1} Na_2SO_4 indicating its high cycling stability. The synthesis route proves to be beneficial for a comprehensive yield of $MnFe_2O_4$@rGO nanosheets of different morphologies for use in the sophisticated design of energy-storing devices. This research strongly suggests that nanoparticle geometry, in addition to two-dimensional carbon-based materials, is a critical factor in a supercapacitor design.

Received 23rd February 2021
Accepted 16th March 2021

DOI: 10.1039/d1na00144b

rsc.li/nanoscale-advances

1. Introduction

Sustainable technologies for energy conversion and storage remain an indispensable part of the current civilization taking into consideration the rising global economy with environmental consciousness. The present rapid depletion of fossil fuels and increasing environmental pollution have prompted the scientific community to focus on delivering green and environmentally friendly research output.[1] In electrochemical energy storage (EES) technology, supercapacitors surpass batteries in many aspects as they possess some exceptional properties like fast recharge capability, high power density, long cycle life over repeated charge–discharge cycling and better endurance. They are diversified in various applications including portable electronic gadgets, power back up, hybrid electric vehicles and several microdevices.[2,3] Motivated by the aforementioned endeavours, multitudinous efforts are being made to increase the quality of the electrode material which plays a pivotal role in the overall efficiency of a supercapacitor. Electrode materials are generally classified into two types: electric double layer capacitors (EDLCs) and pseudocapacitors.

EDLC based supercapacitors have superior specific capacitance but are limited by low energy density as their storage mechanism occurs on the electrode surface at the interface between the electrolyte and electrode *via* electrostatic adsorption of electrical charge. This constricts their broader range of applications, where an appropriate power density is necessary only for a short period of time.[4] Generally, carbon based materials such as graphene, carbon black, graphene oxide, reduced graphene oxide, *etc.*, exhibit EDLC-type behaviour. In the case of pseudocapacitors, a very high energy density is obtained where the charge storage mechanism is due to fast faradaic redox reactions.[5,6] Different types of metal oxides

Department of Nanoscience and Technology, Bharathiar University, Coimbatore 641 046, India. E-mail: ponpandian@buc.edu.in; Tel: +91-422-2428 421

† Electronic supplementary information (ESI) available. See DOI: 10.1039/d1na00144b

including spinel,[7,8] transition metal oxides[9,10] and conducting polymers[11,12] have been reported as pseudocapacitive materials. However, these metal oxides suffer from sluggish ion diffusion problems and poor electrical conductivity resulting in low capacitive performance. Moreover, the inferior structural stability of conducting polymers limits the cycle life of the electrode.[7] To circumvent these challenges, the beneficial features of the individual components of EDLC and pseudocapacitive materials are scrutinized to form a nanocomposite and developed into an efficient active electrode material.[13]

In our work, the pseudocapacitive constituent of the nanocomposite is designed as $MnFe_2O_4$, a spinel ferrite as it is advantageous with the coexistence of two different transition-metal ions Mn and Fe. Also, a rich faradaic redox reaction considering the multiple oxidation states of Mn will meet the requirements of an efficient electroactive component.[14–16] Many research groups have already tried to synthesize $MnFe_2O_4$ by various wet chemical methods including co-precipitation, solvothermal, and template-assisted methods.[17,18] The solvothermal method proves to be advantageous compared to the other wet chemical methods as the working parameters such as pH, temperature, solvent selection, *etc.* could be altered in a wider range.[19] However, the material performance depends on not only the synthesis route but also the morphology, size and microstructure of the sample obtained. Therefore, control over the morphology and uniform size of $MnFe_2O_4$ remains a major focus.[20] Several morphologies of $MnFe_2O_4$ have been developed (spheres, clusters, needles, flakes, *etc.*). We have concentrated mainly on spherical and one-dimensional nanoneedles which were synthesized by altering the working parameters in the hydrothermal method.

Reduced graphene oxide (rGO) is taken as the EDLC component of the working electrode as its spongy wrinkled nature with a high surface area acts as a supportive matrix for $MnFe_2O_4$ to attach itself onto the layered surface. The scarcity of oxygen functional group in rGO compared to graphene oxide (GO) and the increase in C/O ratio above 6 facilitates a faster electron transport processing rGO compared to GO.[21] Therefore, a decrease in the diffusion length of the ions enhances the electrical conductivity in the nanoscale domain thereby improving the effective electrochemical utilization of $MnFe_2O_4$ in the nanocomposite. Recently, research was made towards developing a complete cell for a supercapacitor comprising $MnFe_2O_4$/rGO as the cathode and rGO as the anode, which exhibited a good power density of 750 W kg^{-1} with an energy density of 28.12 W h kg^{-1}. A prominent specific capacitance of 768 F g^{-1} was also attained at a current density of 8 A g^{-1} contributing to the overall performance of the fabricated cell.[16] Another group fabricated a hybrid supercapacitor using a two-electrode system with the $MnFe_2O_4$/rGO nanocomposite which revealed a specific capacitance of 271 F g^{-1} at a current density of 0.5 A g^{-1} with an exceptional cycling durability of 104% after 5000 cycles.[22] To our knowledge, only a few reports on the supercapacitive behaviour of morphology dependent $MnFe_2O_4$ on a carbon matrix (GO, rGO, CNT nanofibers, *etc.*) have been published, a summary of which is in Table 2. Herein, we report the preparation of $MnFe_2O_4$ nanoparticles–rGO nanocomposite and $MnFe_2O_4$ nanoneedles–rGO nanocomposite by a one-pot solvothermal method. The optimum weight percentage of $MnFe_2O_4$ and rGO was fixed before depositing over a stainless steel substrate. To determine the effect of the substrate, copper foil was also taken as an additive substrate. A three electrode set-up was arranged to determine the electrochemical properties of the synthesized materials and their specific capacitance was evaluated by cyclic voltammetric and galvanostatic charge–discharge measurements. The electrochemical performance of the two pristine and rGO nanocomposites of $MnFe_2O_4$ was evaluated by calculating specific capacitance from both cyclic voltammetry and galvanostatic charge–discharge measurements. The Trasatti method was applied to determine the contribution of pseudocapacitance and electric double layer capacitance. The results of power density, energy density and cycling stability demonstrate that the $MnFe_2O_4$ nanorods–rGO nanocomposite could be an optimal choice for supercapacitor electrode material characterized by its high specific capacitance and related properties.

2. Experimental section

2.1 Chemicals and reagents

Graphite powder (325 mesh) and manganese chloride ($MnCl_2 \cdot 4H_2O$) were purchased from Sigma. Ferric chloride ($FeCl_3 \cdot 6H_2O$), sodium hydroxide (NaOH), potassium permanganate ($KMnO_4$), ammonia solution, sodium nitrate ($NaNO_3$), sulfuric acid (H_2SO_4), hydrogen peroxide (H_2O_2) and ethanol were obtained from HiMedia. All the chemicals purchased were of scientific grade and used directly without any purification.

2.2 Synthesis of $MnFe_2O_4$ nanoparticle and nanoneedle structures

The preparation methodology for $MnFe_2O_4$ nanoneedles is reproduced from earlier work with some modifications.[23] For a typical synthesis of $MnFe_2O_4$ nanoneedles named (M-nr), $MnCl_2 \cdot 4H_2O$ and $FeCl_3 \cdot 6H_2O$ were taken in a ratio of 1 : 2 and stirred separately in 20 ml of distilled water until completely dissolved. The iron chloride solution was then added dropwise to the manganese chloride solution and stirred for another 30 minutes. Finally in this protocol, the required weight of NaOH was dissolved separately in 10 ml deionized water and it was added dropwise to the metal salt solution until the pH reached 14. The slurry was then decanted into a Teflon autoclave and kept at 180 °C for 18 hours. The obtained sample was washed with distilled water and ethanol to remove the impurities and finally dried in a vacuum at 80 °C for 6 h. To obtain $MnFe_2O_4$ nanoparticles described henceforth as (M-np), the same procedure was repeated except that the pH was maintained at 12 and the oven temperature was kept at 180 °C for 12 h.

2.3 Synthesis of $MnFe_2O_4$/GO composites

Graphene oxide was synthesized based on a modified Hummer's method involving both the oxidation of the graphite sheets and further exfoliating them to obtain GO sheets as

reported in our earlier work.[24] In a typical process, 10 mg of the as-prepared GO was ultrasonicated in 20 ml DDW solution for several hours forming a uniform yellow-brown suspension. Then, the precursor solution of the respective $MnFe_2O_4$ (nanoparticles or needles) was added slowly to the GO suspension and sonicated for two hours. The mixture was transferred to a Teflon autoclave and refluxed at their respective temperatures mentioned before. The precipitate was rinsed several times and maintained at 80 °C overnight to obtain $MnFe_2O_4$ nanoparticles/rGO and $MnFe_2O_4$ nanoneedles/rGO composites denoted as M-np/rGO and M-nr/rGO respectively. The preparation protocol of the $MnFe_2O_4$ nanocomposites is presented schematically in Scheme 1.

2.4 Characterization

The synthesized $MnFe_2O_4$ structures and their respective GO composites were characterized by using a Rigaku SmartLab X-ray diffractometer with monochromatized Cu $K_{\alpha 1}$ radiation (1.5406 Å) for their crystallographic details. The topographical and morphological information was obtained using a ZEISS, Merlin model Field Emission Scanning Electron Microscope (FESEM) with an accelerating voltage of 5 kV and the elemental analysis was done by energy dispersive X-ray spectroscopy (EDAX). Raman spectroscopy was performed on a Horiba Jobin Yvon LabRam-HR Raman spectrometer with a laser source with an excitation wavelength of 514 nm.

2.4.1. Electrochemical measurements. The electrochemical measurements were carried out on VersaSTAT Princeton Applied Research – AMETEK model. The electrolyte was optimized in 1 M Na_2SO_4 with Ag/AgCl as the reference electrode and Pt as the counter electrode. The working electrode of the four samples was prepared by making a slurry of the respective active material, PVDF (polyvinylidene difluoride) and carbon black in a ratio 8 : 1 : 1 mixed with a drop of *N*-methyl-pyrrolidinone (NMP). The paste was coated uniformly using the doctor blade method onto a stainless steel substrate with a working area dimension of 1 × 1 cm^2. The substrate was weighed before and after coating (dried) to calibrate the accurate mass of the active material coated. To determine the effect of the substrate, copper foil was also used as a substrate with the same dimension. Cyclic voltammetry (CV) from 0.1 to −0.35 V was performed with different scan rates ranging from 5 m to 100 mV s^{-1}. The galvanostatic charge and discharge tests were carried out in the same potential window of CV. Electrochemical impedance spectroscopy (EIS) was performed by applying a frequency range from 1 Hz to 10 kHz.

3. Results and discussion

3.1 Structural and functional group analysis

The crystalline nature and phase identification of the individual morphological components, as well as their respective reduced graphene oxide composites, were analyzed by XRD. Their X-ray diffraction (XRD) profile in the range of $20° < 2\theta < 75°$ with a step size of 0.02° is shown in Fig. 1a. The sharpness of the highest intense peak (311) indicates that the material is highly crystallized without any impurities and its broadness indicates that the crystalline size is very small. The diffraction peaks observed at 2θ of 28.79, 33.5, 35.08, 40.47, 53, and 58.17° represent the Bragg reflections corresponding to the planes (220), (311), (222), (400), (422), (511), (440), (531), and (622) respectively confirming the spinel cubic structure of $MnFe_2O_4$ with the space group $Fd\bar{3}m$ (227) according to the JCPDS card no. 73-1964.[25]

The distinctive peak of graphene oxide at 11.23° signifying the (001) plane is represented in the XRD diffractogram (Fig. S1†). The diffraction peaks for $MnFe_2O_4$/rGO nanocomposites show a low intense peak compared to the pure $MnFe_2O_4$ structures. Graphene related peaks were not observed in the composite which suggests that during the hydrothermal reaction, the GO is well exfoliated for the $MnFe_2O_4$ structures to nucleate and infuse into the graphene layers.[26] Previous results suggest that the reflections of rGO in XRD also diminish due to

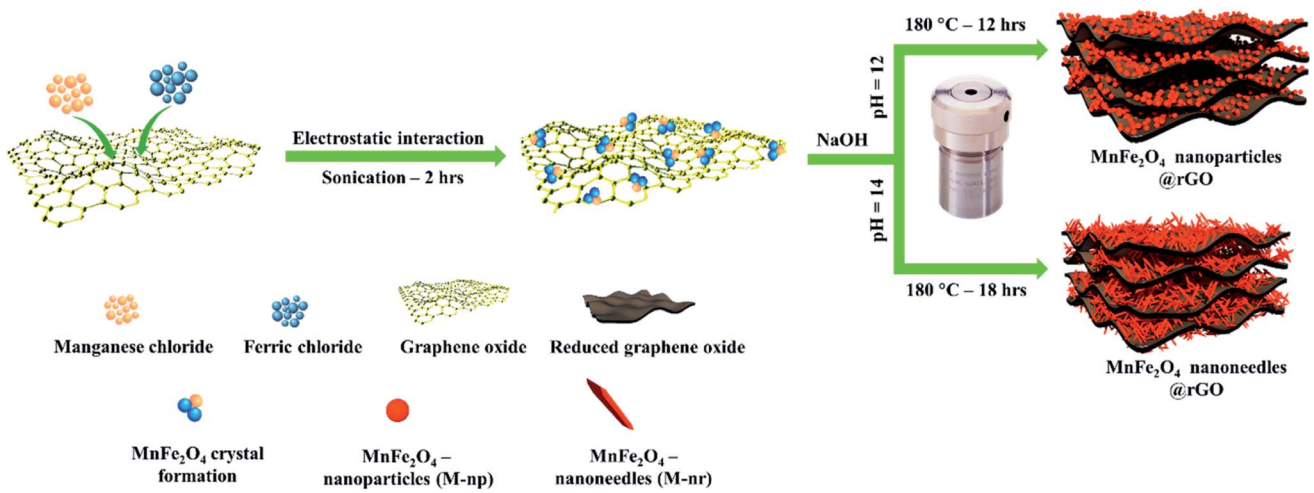

Scheme 1 Schematic illustration of hydrothermal synthesis of morphologically tuned $MnFe_2O_4$/rGO nanocomposites of nanoparticles and nanoneedles.

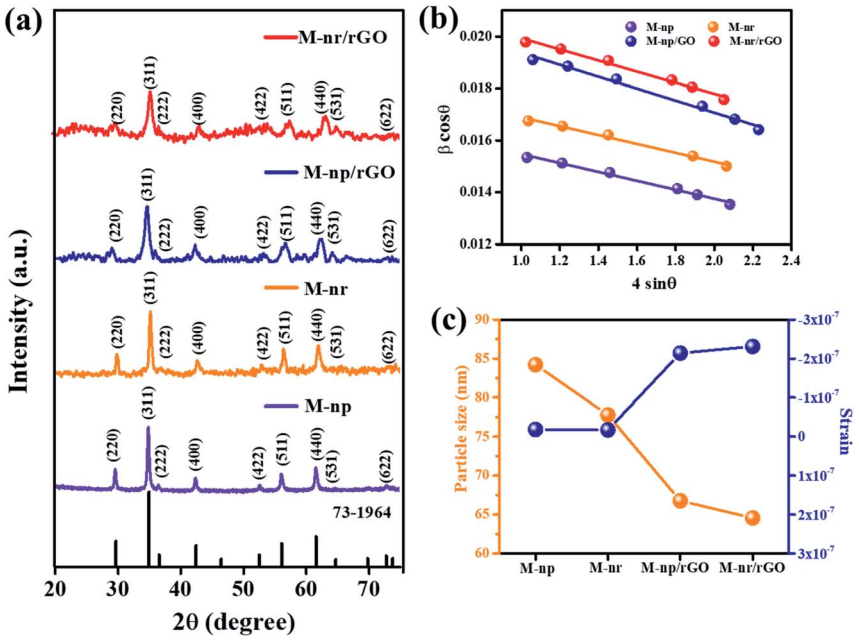

Fig. 1 (a) XRD diffraction pattern of the hydrothermally synthesized $MnFe_2O_4$ nanoparticles: M-np, $MnFe_2O_4$ nanoneedles: M-nr, reduced graphene oxide composite of $MnFe_2O_4$ nanoparticles: M-np/rGO and reduced graphene oxide composite of $MnFe_2O_4$ nanoneedles: M-nr/rGO, (b) Williamson–Hall (W–H) plot of the synthesized samples and (c) the relationship between particle size and strain derived from the Williamson–Hall method.

the ultra-sonication which is further found to be reduced and aggregated into a multilayer structure.[27,28]

The interplanar spacing d_{hkl} was calculated using Bragg's equation for the most prominent plane (311) which further helped to derive the experimental lattice constant from the relationship

$$a_{exp} = d(h^2 + k^2 + l^2)^{1/2} \quad (1)$$

The well-known Scherrer formula was used to determine the average crystalline size of the synthesized $MnFe_2O_4$ structures and nanocomposites[29]

$$D = k\lambda/\beta \cos\theta \quad (2)$$

where k is the shape factor (0.9), and λ, β and θ are the wavelength of the Cu-K_α X-rays (1.5406 Å), full width at half maximum derived from fitting the curve converted to radians and the diffraction angle (in radians) of a specific diffraction peak respectively. The broadening of the diffraction peak is based on the combined effect of the size and the strain developed in the nanostructures.

$$\beta_T = \beta_s + \beta_\varepsilon \quad (3)$$

where β_T is the total broadening, β_s is the broadening due to the size and β_ε the broadening due to strain. By employing the Williamson–Hall (W–H plot) method,[30] both the strain developed (ε) and the grain size (P) could be calculated from the relationship

$$\beta \cos\theta = \varepsilon(4 \sin\theta) + k\lambda/P \quad (4)$$

When plotting 4 sin θ on the x-axis and β cos θ on the y-axis, the gradient (slope) of the line gives the strain (ε) and the grain size (P) can be calculated from the intercept of the line on the y-

Table 1 The d-spacing of the (311) plane (d_{311}), the experimental lattice parameter calculated, the volume of the cubic cell (Å^3), the average crystallize size calculated from the Scherrer formula ($D_{Scherrer}$) and W–H plot ($D_{W-H\ plot}$), and the strain (ε) derived from the slope of the W–H plot. The values in the square brackets represent the estimated error

Samples	Lattice distance (Å)	Lattice parameter (Å) [±0.005]	Lattice volume (Å^3)	Average grain size (nm) [±2 nm]		Strain (ε)
				Scherrer formula	Williamson–Hall plot	
M-np	2.542	8.446	602.494	98	84	-1.834×10^{-8}
M-nr	2.537	8.442	601.639	94	78	-1.72×10^{-8}
M-np/rGO	2.523	8.439	600.997	81	67	-2.14×10^{-7}
M-nr/rGO	2.512	8.435	600.143	77	65	-2.31×10^{-7}

axis by equating it to the known parameters. From Fig. 1b, it is evident that the slopes are negative for all the plots indicating that only a minimum strain is developed.[31] The strain developed is inversely proportional to the grain size which can be seen from Fig. 1c indicating an increase in the interface between the rGO layers. The calculated parameters are tabulated in Table 1. A decreasing trend is seen in the average grain size with the $MnFe_2O_4$ nanoneedle composite (M-nr/rGO) displaying the least value of 77 ± 2 nm. Also, the calculated *d*-spacing value of pure $MnFe_2O_4$ structures (~2.542 Å) is very less compared to that of GO (7.869 Å) signifying that it could very easily impregnate between the graphene oxide layers and it also corresponds well to previously reported values.[32]

Raman spectroscopy is an essential tool to explore the structural properties of the synthesized materials. Fig. 2A shows the Raman spectra of M-np, M-nr, graphene oxide (GO), M-np/rGO and M-nr/rGO nanocomposites. In $MnFe_2O_4$, oxygen atoms at the tetragonal sites are prone to symmetric stretching represented as the A_{1g} mode. The peaks appearing at 560 cm^{-1} in all the spectra except Fig. 2A(c) denotes this A_{1g} mode.[33] In GO, the vibrations of the planar sp^2 carbon atoms denoted as the E_{2g} symmetry (also called the G band) originate at 1592 cm^{-1} as illustrated in Fig. 2A(c). The graphene layer width can be correlated with the decrease in the lattice spacing of the nanocomposites. The band at 1350 cm^{-1} (Fig. 2B) represents the *j*-point phonons of A_{1g} symmetry, also called the D band or the defect band. It corresponds to the defect levels or the agglomeration formed within the graphene layers. The intense D band in the GO spectra is associated with the cleavage of sp^2 bonds to generate more sp^3 bonds.[34,35] The ratio of I_D/I_G is deduced to be 1.45 and 1.46 for M-np/rGO and M-nr/rGO nanocomposites respectively, compared to graphene oxide (0.97) suggesting the reduction of GO to rGO. The ratio of the D band to G band intensity can also be used to determine the in-plane crystallite size (L_a) of the graphene oxide layers as shown in Fig. 2C using the relationship of[36]

$$L_a\ (\text{nm}) = 4.4 \times I_D/I_G \quad (5)$$

The calculated results suggest that the M-nr/rGO nanocomposite has a larger in-plane crystallite size of 6.45 nm compared to the M-np/rGO nanocomposite with 6.38 nm and GO with 4.3 nm respectively. This demonstrates that the GO sheets were well exfoliated during the nanocomposite formation to make room for the $MnFe_2O_4$ structures to disperse well on the layers of GO.

An insight into the morphology and microstructure of the synthesized samples was obtained by FESEM. The morphology of the sample depends purely on the synthesis method and it is substantiated from Fig. 3a and b that $MnFe_2O_4$ nanoparticles are spherical. The diameter of the spherical structure is ~250 nm described in the form of a histogram (Fig. 3c) and the elemental details are confirmed by EDAX analysis (Fig. 3d) and mapping (inset). The needle like morphology of $MnFe_2O_4$ is confirmed from Fig. 3e. The edges of the needle are in a split fashion (Fig. 3f) which is not reported elsewhere. This morphology is more beneficial as the surface area is enhanced in the edges when compared to the spherical nanoparticles. The M-nr samples exhibited a significantly high-aspect ratio with a height profile of ~2.2 μm and a width of ~220 nm.

Fig. 4a reveals the binary composite morphology of $MnFe_2O_4$ nanoparticles and nanoneedles with the rGO sheets. The spherical structure of the nanoparticles is agglomerated with the rGO sheets. In contrast, when a $MnFe_2O_4$ nanoneedle is composited with rGO (Fig. 4b) it retains its morphology as the nanoneedles are interrelatedly spread on the 2-dimensional surface which further promoted the electron transfer and

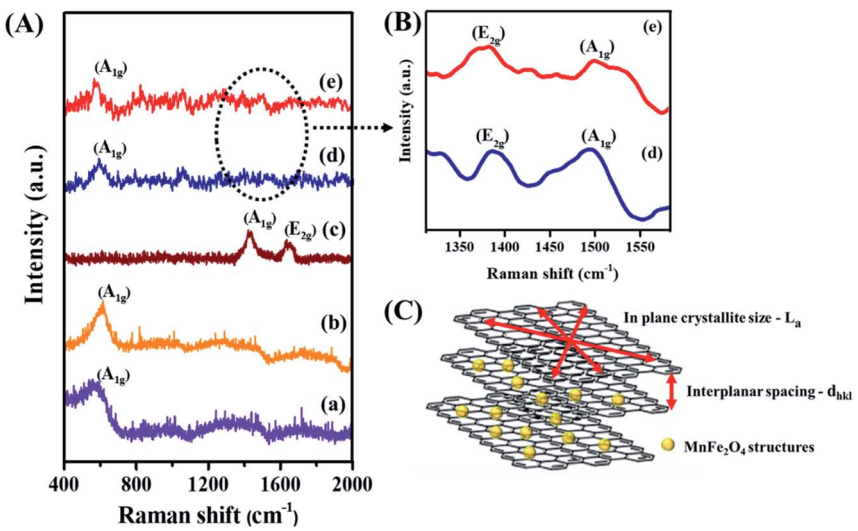

Fig. 2 (A) Raman spectra of (a) $MnFe_2O_4$ nanoparticles: M-np, (b) $MnFe_2O_4$ nanoneedles: M-nr, (c) graphene oxide (GO), (d) reduced graphene oxide composite of $MnFe_2O_4$ nanoparticles: M-np/rGO and (e) reduced graphene oxide composite of $MnFe_2O_4$ nanoneedles: M-nr/rGO, (B) the in-depth view of M-np/rGO and M-nr/rGO representing the reduced graphene oxide peaks and (C) scheme depicting the in-plane crystallite size – L_a in the GO layers during the nanocomposite formation.

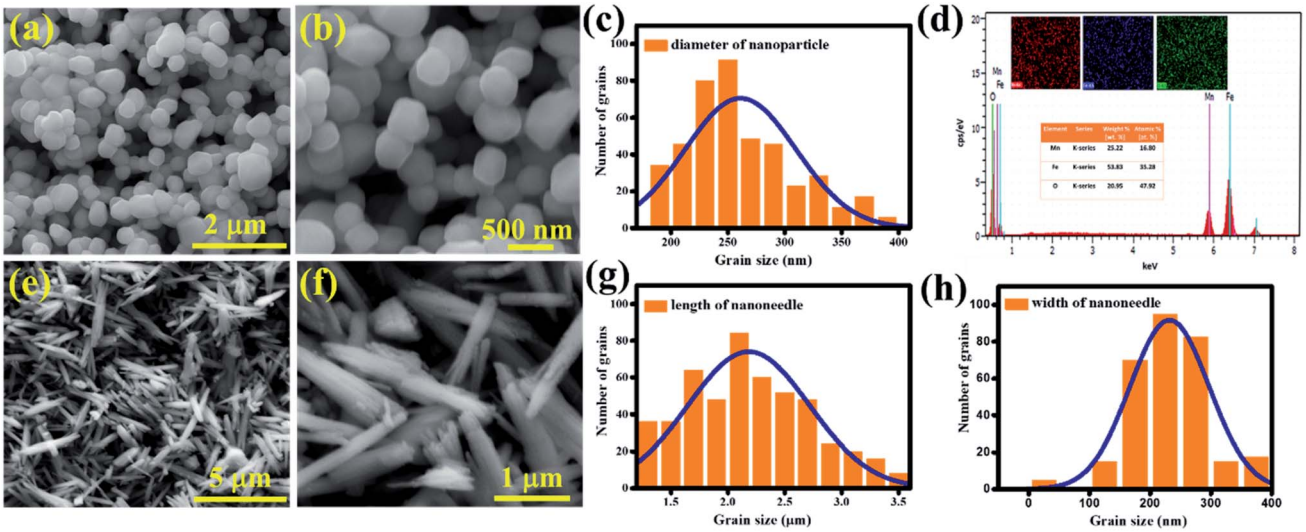

Fig. 3 (a and b) FESEM image of $MnFe_2O_4$ nanoparticles: M-np and (c) histogram of the particle size distribution of M-np, (d) EDX spectra of $MnFe_2O_4$ nanoparticles: M-np (inset shows the corresponding EDS mapping and elemental analysis based on the weight% of Mn, Fe and O present), (e and f) FESEM image of $MnFe_2O_4$ nanoneedles: M-nr and (g and h) histogram of the grain size distribution of M-nr representing the length and width of the nanoneedle.

intensified the active sites thereby suppressing agglomeration.[37] Fig. 4c shows the survey spectrum of the M-nr/rGO sample providing proof for the existence of elements Mn, Fe, O and C. The ratio of atomic contents of Mn and Fe is about 1 : 2 and the carbon content is predominantly from graphene exposed on the surface. Their respective EDS mapping is presented in Fig. 4d.

3.2 Electrochemical properties

For effective practical application as a supercapacitor, the electrochemical performances were evaluated with the aid of a three-electrode system where the respective sample of $MnFe_2O_4$ was employed as the working electrode against Ag/AgCl as the reference and Pt wire as the counter electrode in a 1 M Na_2SO_4 aqueous electrolyte. Initially, the cyclic voltammograms of individual electrodes depicted in Fig. 5a at a constant scan rate of 5 mV s^{-1} clearly show that M-Mn/rGO possesses the maximum area under the CV curve with the maximum current density. This can be ascribed to the differences in the structure and crystalline size between the nanoparticle and needle-like structures of $MnFe_2O_4$ and also due to the synergetic effect of the graphene composite with the ferrite. Also, the contact area between the electrode and the electrolyte as well as the rate of the electrode reaction is enhanced with the graphene architecture incorporated into the 1-D needle like $MnFe_2O_4$ structures.[38] Compared to pure $MnFe_2O_4$ structures, the CV graph of porous graphene oxide recorded in 1 M Na_2SO_4 solution is nearly rectangular in shape. No distinct peaks are observed signifying that the redox reaction is absent and there are no distortions in the curves even at a scan rate of 100 mV s^{-1} (Fig. S3†). This indicates excellent capacitance behaviour and fast diffusion of electrolyte ions into the electrode.[39] Although the integration of a carbon content into the $MnFe_2O_4$ matrix increases the efficacy, that alone is not sufficient to increase the capacitance which is clearly evident from the vast difference in the current densities of M-Np/rGO and M-Mn/rGO. The agglomeration of the $MnFe_2O_4$ nanoparticles (M-Np) onto the rGO demonstrated through FESEM discloses that the transport of electrolytic ions through the electrolyte is compromised leading to the above said issue.[40]

The cyclic voltammograms of M-Mn/rGO between the potential 0.1 and −0.35 V were recorded at various scan rates (5, 10, 20, 50, and 100 mV s^{-1}) as illustrated in Fig. 5b. The area under the curve was found to be proportional to the scan rate. The virtually symmetrical redox peaks indicate good reversibility during charging and discharging and the structure of the CV curve implies that the pseudocapacitive behaviour of the electrode is mainly governed by a faradaic redox reaction. This is attributed to the intercalation/extraction of Na^+ ions from the electrolyte at low scan rates as slow faradaic reactions contribute to more active sites from the inner surface of the working electrode for charge storage. The Na^+ ions interact with the $MnFe_2O_4$ structures in the electrolyte by a redox couple reaction which is reversible as shown in eqn (6):[27,41]

$$x\mathrm{Na}^+ x\mathrm{e}^- + \mathrm{MnFe_2O_4} \Leftrightarrow \mathrm{Na}_x\mathrm{MnFe_2O_4} \quad (6)$$

Fig. 5f shows the specific capacitance and areal capacitance of the active electrode material acquired from CV curves at different scan rates using the relationship:

$$C_s = \frac{1}{2mv(E_f - E_i)} \int_{E_i}^{E_f} I(E)\mathrm{d}t \quad (7)$$

$$C_a = \frac{1}{2Av(E_f - E_i)} \int_{E_i}^{E_f} I(E)\mathrm{d}t \quad (8)$$

where 'C_s' symbolizes the specific capacitance (F g^{-1}), '$E_f - E_i$' indicates the potential window, 'v' indicates the scan rate in

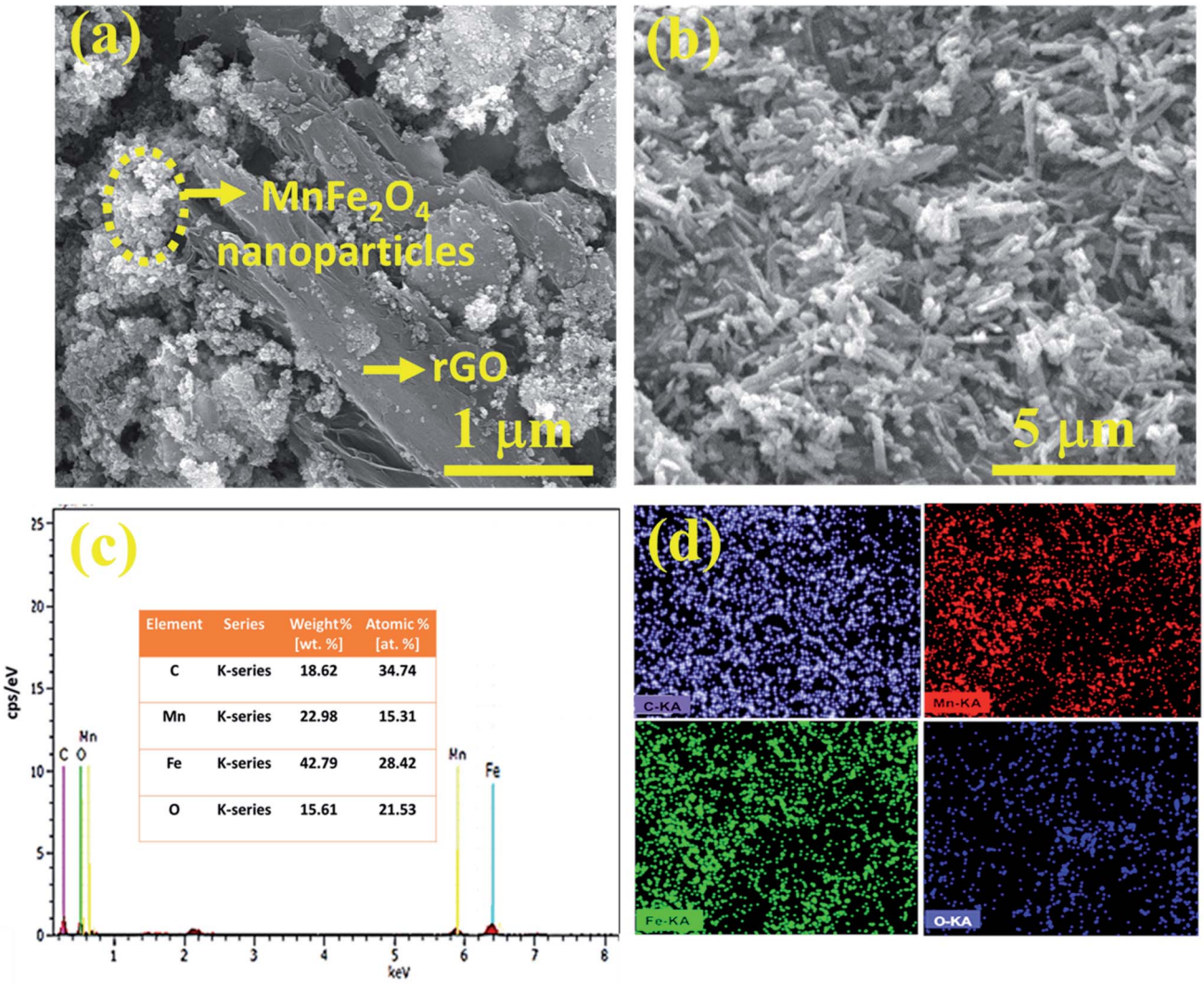

Fig. 4 FESEM image of the (a) rGO nanocomposite of $MnFe_2O_4$ nanoparticles: M-np/rGO and (b) nanocomposite of $MnFe_2O_4$ nanoneedles: M-nr/rGO, (c) EDX spectra of the $MnFe_2O_4$ nanoneedle composite: M-nr/rGO (inset shows the elemental analysis based on the weight% of C, Mn, Fe and O present) and (d) the corresponding EDS mapping of the M-nr/rGO composite.

volts (V), $I(E)dt$ indicates the area under the CV curve of M-Mn/rGO immersed in 1 M Na_2SO_4 solution and 'm' specifies the active mass deposited on the stainless steel substrate in 'g'. 'C_a' represents the areal capacitance (F cm^{-2}) and 'A' is the geometric area set at 1×1 cm^2 in this electrochemical study.

A maximum specific capacitance of 1327 F g^{-1} and an areal capacitance of 890 mF cm^{-2} were observed at the lowest measured scan rate of 5 mV s^{-1} (Fig. 5f). The active sites in the $MnFe_2O_4$/rGO nanoneedles are explored more as the permeable surface structure is beneficial to enrich the electrochemical behaviour. At a lower scan rate, a higher capacitance value is guaranteed as the electrode is fully diffused by Na^+ ions due to more time utilization. In contrast, a low specific capacitance at a higher scan rate is an outcome of the restriction of the same ions due to time limitation. The specific capacitance of all the working electrodes is demonstrated in Fig. S4.† The lower values of the specific capacitance of pure $MnFe_2O_4$ np and nr may be due to the surface adsorption charge storage mechanism and intrinsically poor electronic conductivity of the electrode and these two prominent factors are related to the average crystallite size of the structures calculated by XRD. The grain size is directly proportional to the electronic conductivity and inversely proportional to the specific surface area.[42–44] Therefore tailoring the synthesis parameters to tune the shape and crystallite size of the material promotes optimum electrochemical properties.

To detect the origin of capacitive behaviour at a fundamental level, the Trasatti method was employed to explore the contribution of double-layer capacitance and pseudocapacitance towards the overall specific capacitance.[44,45] The surface capacitive effect is due to the exterior electrochemical sites specified by the direct exposure of the electrode and electrolyte whereas the diffusion-controlled intercalation process is from the interior regions of flaws such as cracks, cavities, fissures and fractures in the grain boundaries.[46] The current response $i(V)$ at

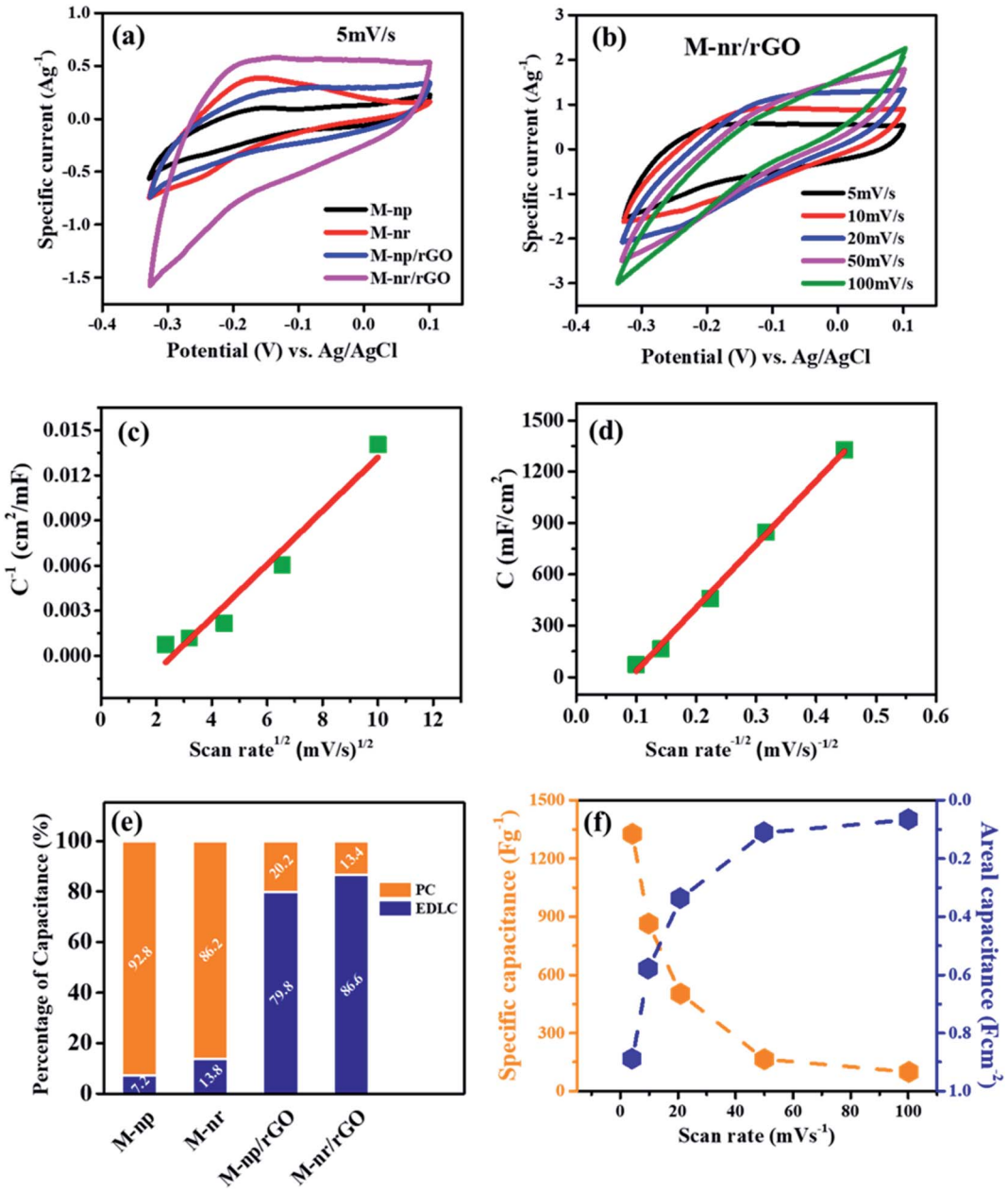

Fig. 5 (a) Cyclic voltammograms of $MnFe_2O_4$ nanoparticles, $MnFe_2O_4$ nanoneedles, $MnFe_2O_4$/rGO nanoparticles and $MnFe_2O_4$/rGO nanoneedles at a constant scan rate of 5 mV s^{-1}, (b) CV of M-nr/rGO at various scan rates extending from 5 to 100 mV s^{-1}, (c) a linear fit of reciprocal of areal capacitance (C^{-1}) *vs.* square root of scan rate ($v^{1/2}$) of M-nr/rGO, (d) linear fit of gravimetric capacitance (C) *vs.* reciprocal of square root of scan rate ($v^{-1/2}$) of M-nr/rGO, (e) percentage of capacitance contribution evaluated for all the samples based on Trasatti analysis, and (f) the plot of specific capacitance *vs.* areal capacitance of M-Mn/rGO as a function of scan rate.

a fixed scan rate as a combination of these two effects can be expressed as:

$$i(V) = k_1 v + k_2 v^{1/2} \quad (9)$$

$$i(V)/v^{1/2} = k_1 v^{1/2} + k_2 \quad (10)$$

Here, $k_1 v$ corresponds to the surface capacitive effect and $k_2 v^{1/2}$ is related to the diffusion-controlled insertion process, where k_1 and k_2 are the scan rate independent constants and v is the scan rate respectively. The scan rate dependence of the current can be derived by dividing both sides with the square root of the scan rate as shown in eqn (10). The total capacitance (C_t) involving the double-layer charging (EDLC) and faradaic pseudocapacitance (PC) (Fig. 5e) can be assessed by extrapolating the linear fit obtained from the reciprocal of areal capacitance 'C^{-1}' *versus* '$v^{1/2}$' (Fig. 5c) presuming 'v' goes to zero. In contrast, the surface capacitance 'C_{sur}' can be studied from 'C' *versus* '$v^{-1/2}$' (Fig. 5d) assuming 'v' goes to infinite. Then, the contribution of capacitance insertion 'C_{ins}' can be naturally resolved from the

difference in 'C_t' and 'C_{sur}' as $C_{ins} = C_t - C_{sur}$.[47] The estimated results from Fig. 5e suggest that pristine $MnFe_2O_4$ electrodes have pronounced pseudocapacitance while the electric double layer capacitance oppresses the capacitance of all rGO composited samples. We find that the faradaic pseudo-capacity contributed 7.2, 13.8, 79.8 and 86.6% whereas the double-layer charging contributed 92.8, 86.2, 20.2 and 13.4% for M-np, M-nr, M-np/rGO and M-nr/rGO electrodes respectively. Taken together, the outcome obtained proves that the faradaic reactions characteristically have relatively slow kinetics, whereas the ion adsorption formed by the electric double layer ensures good rate capability for ultrafast charging/discharging.[48]

To evaluate the storage capability of all the electrodes in the three-electrode system, the electrochemical performance concerning charge and discharge behaviour was determined at a constant current density of 0.5 A g^{-1} (Fig. 6a) with voltage between 0.1 and −0.35 V. The specific capacitance or gravimetric capacitance, 'C_s', and the coulombic efficiency, 'η', from galvanostatic charge–discharge were calculated using eqn (11) and (12) respectively.

$$C_s = \frac{I \times \Delta t}{m(E_f - E_i)} \quad (\mathrm{F\ g^{-1}}) \tag{11}$$

$$\eta = \frac{t_d}{t_c} \times 100\% \tag{12}$$

Here 'I' indicates the respective current density (A g^{-1}),'Δt' is the discharge time in seconds (s) eliminating the IR-drop, 'm' indicates the active mass deposited on the single electrode in 'g' and '$E_f - E_i$' denotes the potential scale during the charge–discharge measurement. The discharging and charging time are represented by t_d and t_c respectively. The capacitance calculated from the GCD curves of Fig. 6a is 950, 876, 720, 536 and 380 F g^{-1} for $MnFe_2O_4$/rGO nanoneedles, $MnFe_2O_4$/rGO nanoparticles, GO, $MnFe_2O_4$ nanoneedles and $MnFe_2O_4$ nanoparticles at 0.5 A g^{-1} respectively. As expected, the $MnFe_2O_4$/rGO nanoneedle composite displays the longest discharge time demonstrating the highest specific capacitance of 950 F g^{-1} at 0.5 A g^{-1} which is in accordance with the CV analysis. The robust electrochemical performance of the $MnFe_2O_4$/rGO nanoneedle sample whose specific capacitance is nearly 2.5 times that of the $MnFe_2O_4$ nanoparticles at 0.5 A g^{-1} is attributed to (i) the presence of reduced graphene oxide in the ferrite sample, which exhibits an integrated large electrical conductivity due to the enhanced specific surface area, (ii) the remaining oxygenated species present in rGO which promotes faradaic capacitance[49] and (iii) the contact between $MnFe_2O_4$ and layered rGO which boosts the electrode–electrolyte interface thereby decreasing the migration path of the ions (Na^{2+}) for better electrolyte infiltration.[50]

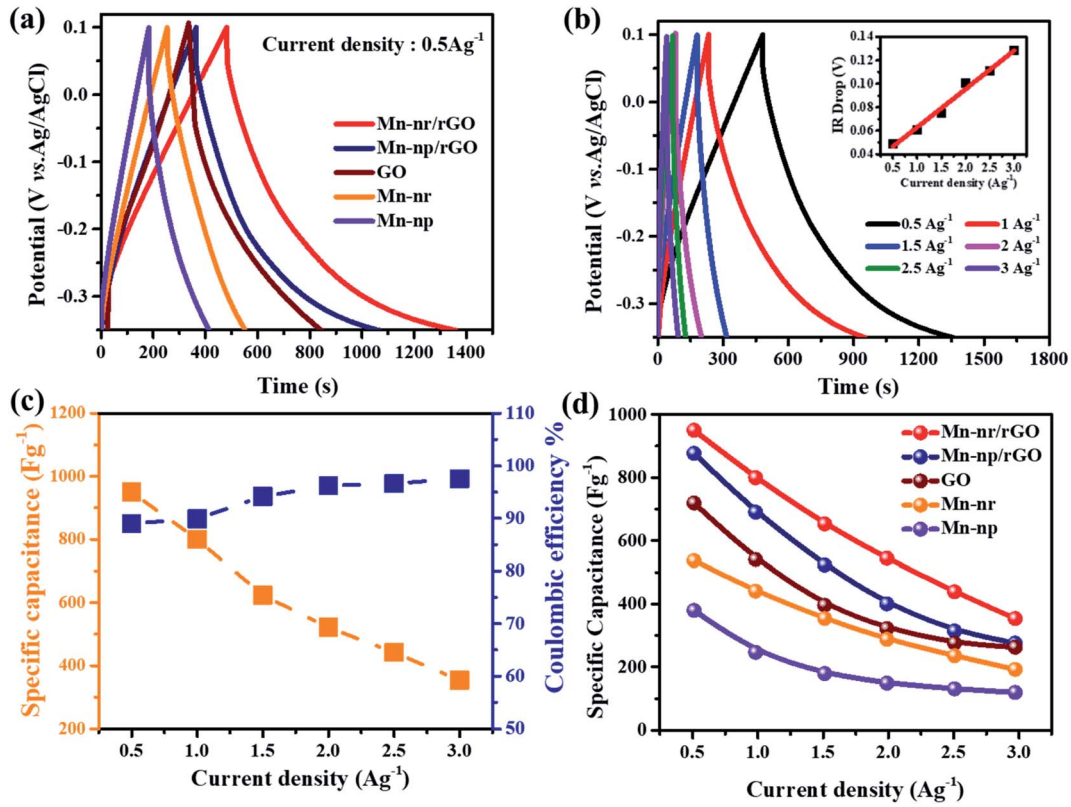

Fig. 6 (a) Galvanostatic charge–discharge curves of $MnFe_2O_4$ nanoparticles, $MnFe_2O_4$ nanoneedles, $MnFe_2O_4$/rGO nanoparticles and $MnFe_2O_4$/rGO nanoneedles at a constant current density of 3 A g^{-1}, (b) GCD of M-nr/rGO at various current densities from 0.5 to 3 Ag^{-1}, (c) the plot of specific capacitance *vs.* coulombic efficiency of M-Mn/rGO as a function of current density, and (d) the calculated specific capacitance of all the samples fitted at different current densities.

Good rate capability and coulombic efficiency are the main criteria to evaluate the practical application of a supercapacitor. Fig. 6b shows the GCD performance of the $MnFe_2O_4$/rGO nanoneedle composite from 0.5 to 3 A g^{-1} with a difference in current density of 0.5 A g^{-1}. It can be seen that the charge–discharge curves at all the current densities are dimensionally symmetrical with a trivial IR drop indicating small internal resistance and better reversibility of the electrode.[51] The IR drop in the Fig. 6b inset showed a linear increase from 0.04 Ω to 0.12 Ω with increasing current density. The specific capacitance of the composite electrode scaled to 950 F g^{-1} at 0.5 A g^{-1} demonstrated a high coulombic efficiency of ~97.5% and retained a capacitance of 354 F g^{-1} at 3 A g^{-1} with an efficiency of 89% suggesting admirable rate performance (Fig. 6c). In contrast, for pristine $MnFe_2O_4$ nanoparticles, the specific capacitance decreased from 380 F g^{-1} to 118 F g^{-1} signifying a very low capacitive retention rate. The interface between the rGO layer and pristine $MnFe_2O_4$ serves as a reason for the synergistic effect between the pseudocapacitance and the electric-double layer mechanism.[52] Moreover, the active surface area of 1-D $MnFe_2O_4$ nanoneedles compared to that of the $MnFe_2O_4$ nanoparticles provides high exposure of electroactive sites for rapid diffusion of ions demonstrating good rate capability and high specific capacitance of the $MnFe_2O_4$ nanoneedle composite electrode. The specific capacitance of pristine and composite electrodes of $MnFe_2O_4$ is calculated, compared and illustrated in Fig. 6d.

Electrochemical impedance spectroscopy (EIS) of $MnFe_2O_4$/rGO nanoneedles which exhibited superior electrochemical properties was performed at room temperature to determine the electrode's fundamental behaviour in the electrolyte. The Nyquist plot before and after charging for 5000 cycles is shown in Fig. 7a. The spectra show a semicircle that intersects the real axis in the high-frequency region, where the resistance (R_s) in the ionic conductivity of the electrolyte system is enlarged in the inset. The mid and the low-frequency region reveal a virtually vertical line around 45° called the Warburg element which distinguishes an electrode with high porosity and capacitance.[53] A smaller value of R_s is advantageous for better ionic conduction and decreasing the ohmic losses.[54] The R_s value increased from 0.56 Ω to 0.94 Ω after 2000 cycles (Fig. 7a inset) indicating a diminution in the overall electrochemical behaviour of the electrode material.

Furthermore, an important constraint to determine the power capability of a capacitor is the "Knee frequency" where a shift occurs from the high frequency to the low frequency component.[54] The knee frequency value before charging was 233 Hz, signifying that the electrode could be operated up to 233 Hz to utilize its capacitive properties. The value decreased to 136 Hz after charging for 5000 cycles.

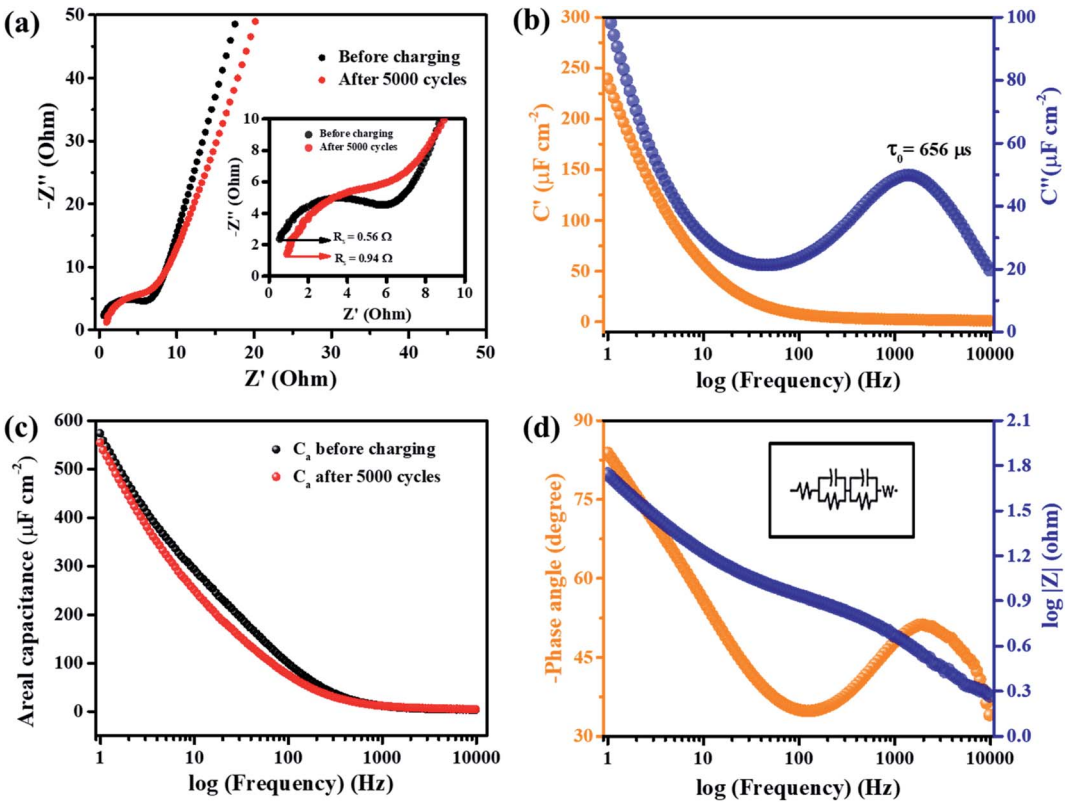

Fig. 7 (a) The EIS impedance spectra of M-nr/rGO before charging and after 2000 cycles (the inset shows the internal resistance), (b) the real component C' and the imaginary component C'' plot *vs.* frequency of M-nr/rGO, (c) the calculated specific capacitance of the M-nr/rGO nanocomposite from the impedance spectra before and after charging and (d) the phase angle Bode plot and impedance Bode plot of the M-nr/rGO nanocomposite.

The areal capacitance, C_a, from EIS was calculated using the relationships,

$$C_a = \frac{C(\omega)}{2\pi r^2} \quad (\mathrm{F\ cm^{-2}}) \tag{13}$$

$$C(\omega) = C'(\omega) + C''(\omega) \tag{14}$$

$$C'(\omega) = \frac{-Z''(\omega)}{\omega|Z|^2} \text{ and } C''(\omega) = \frac{-Z''(\omega)}{\omega|Z|^2} \tag{15}$$

$$|Z| = \sqrt{(Z')^2 + (Z'')^2} \tag{16}$$

where $C(\omega)$ represents the total capacitance, $C'(\omega)$ and $C''(\omega)$ denote the real and imaginary capacitance components respectively, $Z'(\omega)$ and $Z''(\omega)$ represent the real and imaginary impedance components respectively, and 'ω' is the angular frequency ($2\pi f$), where 'f' is the frequency in Hz and $|Z|$ is the modulus of Z. Here $r = 1$ cm as the mass loading area has a dimension of 1×1 cm^2. The total capacitance obtained from EIS is a combination of both the real and the imaginary part of the capacitance (eqn (14)). While the real component, $C'(\omega)$, is the charge stored as a function of frequency depending mainly on the porosity of the material taken, the mass loading and the nature of the electrolyte, the imaginary component, $C''(\omega)$, denotes the dissipation of energy during the storage of charge. C' and C'' *versus* frequency in Hz are plotted in Fig. 7b, where the specific capacitance obtained is in microfarads. These values are incomparable with the previously calculated specific capacitance from CV and GCD curves because, during EIS measurements, immobility occurs due to the confinement of ions in the electrolyte solution.[54] Moreover, to determine the rate of charge–discharge performance of an electrode, the relaxation time τ_o (s) is calculated from the imaginary part of the capacitance (C'') with the relationship, $\tau_o = 1/f_o$, where f_o (Hz) is the peak point in the high frequency region. A very less value of 656 μs was in accordance with previously reported values,[16,22,55] suggesting that only a minimum time is required to discharge all the energy from the electrode.

The areal capacitance of the composite electrode before and after charging is plotted *versus* the log of frequency (Hz) from eqn (13) and demonstrated in Fig. 7c. The calculated areal capacitance starts with a value of 3.5 μF cm^{-2} at 10 kHz in both cases indicating that the resistive nature of the electrode does not change even after charging. In contrast, the capacitance

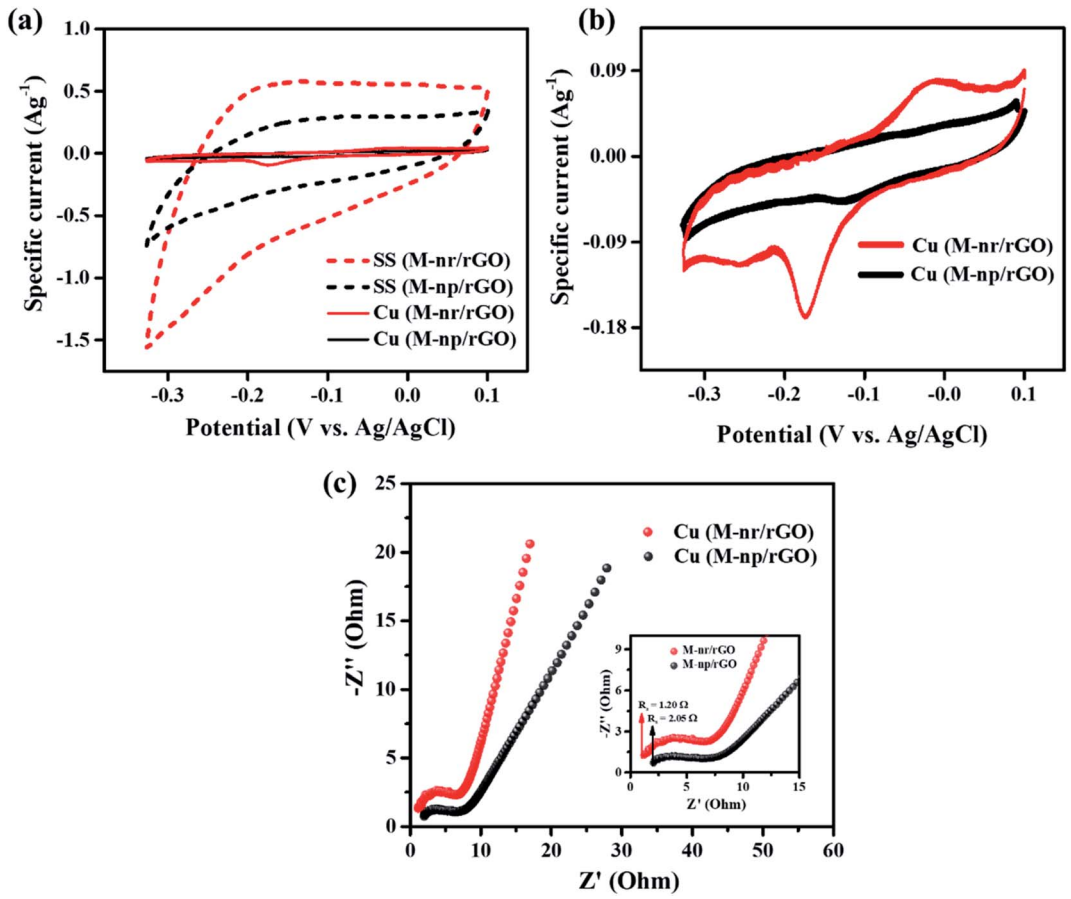

Fig. 8 (a) Cyclic voltammograms of $MnFe_2O_4$/rGO nanoneedles and $MnFe_2O_4$/rGO nanoparticles deposited on stainless steel (SS) and copper (Cu) substrates respectively at a constant scan rate of 5 mV s^{-1}. (b) The cyclic voltammograms of $MnFe_2O_4$/rGO composites deposited on a copper substrate enlarged to describe the actual specific current attained. (c) The EIS impedance spectra of Cu (M-nr/rGO) and Cu (M-np/rGO) (the inset presents the internal resistance of both the samples).

increases to 573 μF cm^{-2} for the electrode before charging and a slightly less capacitance value is seen in the mid and low frequency regions of the electrode after charging, which matches with the R_s values and knee frequency values mentioned earlier.

The Bode plots of the phase angle and total impedance $|Z|$ *versus* frequency (Hz) are shown in Fig. 7d with the equivalent circuit presented in the inset. The graph implies that the phase angle (Φ) in the lower frequency region is −84° confirming the capacitive properties of the electrode ($\Phi = 0°$) for an ideal resistor and ($\Phi = 90°$) for an ideal supercapacitor in the low frequency region.[54] The impedance Bode plot shows inclination in the low frequency region (LF), the mid-frequency region (MF) and the high frequency region (HF). The slope values were in the order of LF (1–50 Hz) > HF (500–1000 Hz) > MF (50–500 Hz) (Fig. S5†). The high slope value in the LF region is possibly due to the resistive behaviour at the interfaces, and the HF regions combine the characteristics of both the resistive and the capacitive component, but the least slope value in the MF regions depicts purely the capacitive nature of the electrode.[56]

To understand the substrate dependency concerning the electrochemical performance of the synthesized $MnFe_2O_4$ samples, the $MnFe_2O_4$/rGO composites comprising nanoneedles and nanoparticles were deposited on copper foil with no modification in any other parameters. The samples were labelled with the prefix Cu and SS for copper foil and stainless steel substrates respectively. From the cyclic voltammetry test depicted in Fig. 8a and b, the area under the curve of the samples deposited on the Cu substrate is drastically less compared to that of the previously available results of the SS substrate. The enlarged view of $MnFe_2O_4$/rGO composites deposited on the copper substrate is shown in Fig. 8b, where the maximum specific current obtained is only 0.09 A g^{-1}. The rationale behind this is that copper ions on the substrate tend to react with the electrolyte, which leads to the diffusion of ions within the electrode. This increases the total resistance of the system thereby hindering the overall stability of the electrode.[57,58] Fig. S6† illustrates the cyclic voltammograms of $MnFe_2O_4$/rGO nanoneedles and nanoparticles deposited on the Cu substrate recorded at various scan rates from 5 to 100 mV s^{-1}. It is clear from the CV profile that both the composite samples exhibit redox peaks different from the ideal rectangular shape for double-layer capacitance revealing that the samples deposited on the copper substrate possess pseudocapacitance properties.[59] The impedance spectra shown in Fig. 8c describe the certainty that the R_s value has almost doubled to 1.20 Ω (for Cu(M-Mr/rGO)) and tripled to 2.05 Ω (for Cu(M-Mp/rGO)) compared to SS(M-Mr/rGO) (from Fig. 7a), revealing an escalation in ohmic losses.

The overall performance of the $MnFe_2O_4$/rGO binary composite is investigated by calculating the energy density (W h kg^{-1}) and power density (W kg^{-1}) using the relationships (17) and (18) as represented in the Ragone plot in Fig. 9a.

$$E = \frac{C_s(E_f - E_i)^2}{2} \times \frac{1000}{3600} \ (\text{W h kg}^{-1}) \quad (17)$$

$$P = \frac{E \times 3600}{\Delta t} \ (\text{W kg}^{-1}) \quad (18)$$

where C_s is the specific capacitance obtained from GCD, $E_f - E_i$ is the potential window after eliminating the IR-drop and Δt is the discharge time. It is clear from the Ragone plot that the M-nr/rGO composite meets the required standards of an electrochemical supercapacitor. Interestingly, the composite provided a maximum energy density of 28 W h kg^{-1} at a power density of 1.67 kW kg^{-1}, which is comparable with or superior to that of other carbon based composites of spinel ferrites (summarized in Table 2). Though energy densities reduced slowly with increasing power densities, it managed to maintain 5.7 W h kg^{-1} at a power density of 10 kW kg^{-1}, indicating the excellent energy storage ability of the device.[60]

To further assess the potential of the composite for effective practicability of a supercapacitor device, the cycling stability of M-nr/rGO was evaluated by reiterating the GCD and CV tests at a current density of 1.5 A g^{-1} and a scan rate of 5 mV s^{-1}

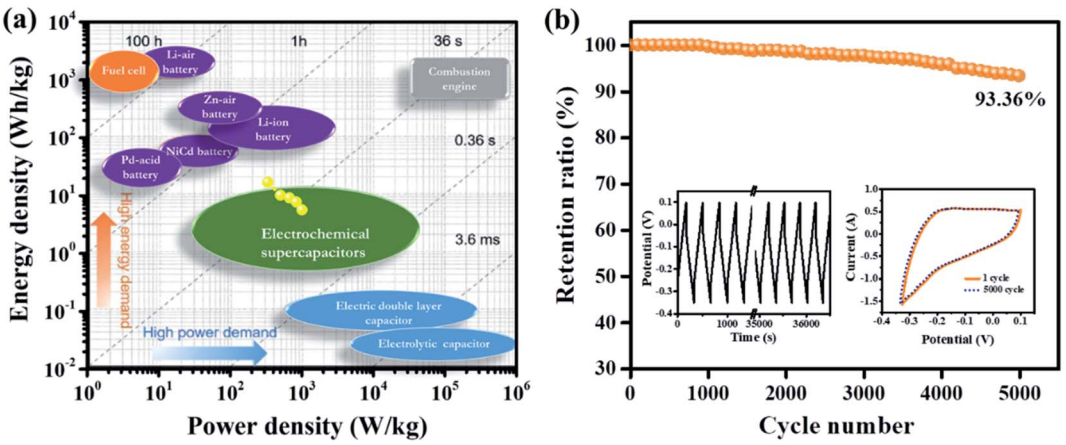

Fig. 9 (a) The Ragone plot for $MnFe_2O_4$/rGO nanoneedles (background adapted from ref. 46) and (b) cycling stability of $MnFe_2O_4$/rGO nanoneedles for 5000 cycles (inset shows the galvanostatic charge–discharge curves for a different number of cycles and CV taken at 1.5 A g^{-1} and 5 mV s^{-1} respectively after completing the 5000 cycles).

Table 2 Comparison for the electrochemical performances of $MnFe_2O_4$ based materials with the existing literature for supercapacitor applications

Sample	Synthesis method	Electrolyte	Specific capacitance ($F\ g^{-1}$)	Energy density ($W\ h\ kg^{-1}$)	Power density ($kW\ kg^{-1}$)	Rate capability/retention	Ref.
$MnFe_2O_4$NPs	Thermal decomposition	2 M KOH	25.21 at (50 mV s^{-1})	12.60	0.74	—	62
$MnFe_2O_4$ microspheres	Solvothermal	2 M KOH	88.4 at (0.01 A g^{-1})	—	—	69.2% after 2000 cycles	63
$MnFe_2O_4$ nanocube	Hydrothermal	1 M NaCl	32 at (0.5 mA cm^{-2})	—	—	—	55
MnO_2/CNT	Co-precipitation	1 M Na_2SO_4	201 at (1 A g^{-1})	3.3	6	100% after 10 000 cycles	64
$MnFe_2O_4$/carbon black	Co-precipitation	1 M NaCl	~55 at (200 mV s^{-1})	7.6	0.11	100% after 3000 cycles	65
PANI/$MnFe_2O_4$	Hydrothermal	1 M H_2SO_4	371 at (1 A g^{-1})	—	—	86.7% after 2000 cycles	66
$MnFe_2O_4$/graphene/PANI	Chemical oxidative polymerization method	1 M NaCl	338 at (0.5 mA cm^{-2})	10.25	3.07	100% after 2000 cycles	55
$MnFe_2O_4$/graphene	Solvothermal	1 M H_2SO_4	120 at (0.1 A g^{-1})	5	0.4	105% after 5000 cycles	67
$MnFe_2O_4$/rGO	Chemical oxidation/sonication	6 M KOH	271 at (0.5 A g^{-1})	15.9	3.24	104% after 5000 cycles	38
$MnFe_2O_4$ hollow sphere/rGO	Hydrothermal	3 M KOH + 0.1 M $K_4[Fe(CN)_6]$	768 at (8 A g^{-1})	27.7	7.5	95% after 4000 cycles	16
$MnFe_2O_4$ nanoneedles/rGO	Hydrothermal	1 M Na_2SO_4	1327 at (5 mA cm^{-2})	5.7	10	93.36% after 5000 cycles	This work

respectively. Fig. 9b reveals that the binary composite has retained 93.36% of its initial capacitance after 5000 GCD cycles indicating remarkably good cycling stability to be implemented in a supercapacitor. Cyclic voltammetry was also performed to determine its electrochemical activation process after cycling. The M-nr/rGO binary composite has achieved this remarkable electrochemical performance due to the mechanically robust hierarchical architecture of 1-dimensional nanoneedles in the spinel type $MnFe_2O_4$ along with the high conductivity of graphene in its reduced form.[61] Furthermore, the electrochemical properties of M-nr/rGO significantly surpassed those in other similar literature described in (Table 2).

4. Conclusion

In summary, two different morphologies of $MnFe_2O_4$ and their respective composite with rGO were synthesized by a facile method for high performance supercapacitor application. The planar structure of rGO aided the unique morphologies of $MnFe_2O_4$ to permeate into the layers forming a stacked 2D/3D structure. The synthesized samples were characterized by different physical methods to determine their physicochemical properties and their electrochemical performance was also evaluated. However, owing to the synergistic effect of unique 1D $MnFe_2O_4$ nanoneedles integrated with 2D-rGO, a higher specific capacitance of 1327 F g^{-1} with an exceptionally high areal capacitance of 890 mF cm^{-2} at a current density of 5 mA cm^{-2} was demonstrated. Also, a remarkable power density of 10 kW kg^{-1} with a retention of 93.36% of the initial capacitance was obtained after 5000 cycles in 1 M Na_2SO_4, indicating high cycling stability. To the best of our knowledge, this is the first time a needle like morphology of $MnFe_2O_4$ is composited with rGO and reported for a supercapacitor application. The results suggest that $MnFe_2O_4$ nanoneedle@rGO is a very promising electrode material for assembling in a capacitor with both high energy and good capacitance retention.

Conflicts of interest

There are no conflicts to declare in the present manuscript.

Acknowledgements

The authors thank the DST-SERB for the funding [EMR/2016/007676] as well as the DST-FIST DST-PURSE, UGC-SAP, Government of India for the support of instrumental facilities available in the department.

References

1 E. Pomerantseva, F. Bonaccorso, X. Feng, Y. Cui and Y. Gogotsi, *Science*, 2019, **366**(6468), eaan8285.
2 P. Simon, Y. Gogotsi and B. Dunn, *Science*, 2014, **343**, 1210–1211.
3 L. Kouchachvili, W. Yaïci and E. Entchev, *J. Power Sources*, 2018, **374**, 237–248.

4 X. You, M. Misra, S. Gregori and A. K. Mohanty, *ACS Sustainable Chem. Eng.*, 2018, **6**, 318–324.
5 L. Huang, B. Liu, H. Hou, L. Wu, X. Zhu, J. Hu and J. Yang, *J. Alloys Compd.*, 2018, **730**, 71–80.
6 L. Miao, Z. Song, D. Zhu, L. Li, L. Gan and M. Liu, *Mater. Adv.*, 2020, **1**, 945–966.
7 F. M. Ismail, M. Ramadan, A. M. Abdellah, I. Ismail and N. K. Allam, *J. Electroanal. Chem.*, 2018, **817**, 111–117.
8 P. Sun, N. Li, C. Wang, J. Yin, G. Zhao, P. Hou and X. Xu, *J. Power Sources*, 2019, **427**, 56–61.
9 X. Cheng, Z. Pan, J. Yang, Y. Zhong, X. Wang, C. Ye, J. Zhuang, Q. Huang, Q. Yongcai and W. Li, *J. Power Sources*, 2019, **427**, 243–249.
10 C. An, Y. Zhang, H. Guo and Y. Wang, *Nanoscale Adv.*, 2019, **1**, 4644–4658.
11 H. Souri and D. Bhattacharyya, *ACS Appl. Mater. Interfaces*, 2018, **10**, 20845–20853.
12 Y. Wang, Y. Ding, X. Guo and G. Yu, *Nano Res.*, 2019, **12**, 1978–1987.
13 Y. Dong, J. Zhu, Q. Li, S. Zhang, H. Song and D. Jil, *J. Mater. Chem. A*, 2020, **8**, 21930–21946.
14 P. Xiong, C. Hu, Y. Fan, W. Zhang, J. Zhu and X. Wang, *J. Power Sources*, 2014, **266**, 384–392.
15 W. H. Low, P. S. Khiew, S. S. Lim, C. W. Siong and E. R. Ezeigwe, *J. Alloys Compd.*, 2019, **775**, 1324–1356.
16 P. Makkar and N. N. Ghosh, *ACS Appl. Energy Mater.*, 2020, **3**, 2653–2664.
17 M. M. Baig, M. A. Yousuf, P. O. Agboola, M. A. Khan, I. Shakir and M. F. Warsi, *Ceram. Int.*, 2019, **45**, 12682–12690.
18 A. Mary Jacintha, V. Umapathy, P. Neeraja and S. Rex Jeya Rajkumar, *J. Nanostruct. Chem.*, 2017, **7**, 375–387.
19 M. Shandilya, R. Rai and J. Singh, *Adv. Appl. Ceram.*, 2016, **115**, 354–376.
20 C. Burda, X. Chen, R. Narayanan and M. A. El-Sayed, *Chem. Rev.*, 2005, **105**, 1025–1102.
21 P. Miao, J. He, Z. Sang, F. Zhang, J. Guo, D. Su, X. Yan, X. Li and H. Ji, *J. Alloys Compd.*, 2018, **732**, 613–623.
22 A. Goljanian Tabrizi, N. Arsalani, A. Mohammadi, H. Namazi, L. Saleh Ghadimi and I. Ahadzadeh, *New J. Chem.*, 2017, **41**, 4974–4984.
23 L. Zhen, K. He, C. Y. Xu and W. Z. Shao, *J. Magn. Magn. Mater.*, 2008, **320**, 2672–2675.
24 N. D. Navadeepthy, R. A. Rebekah, V. C. Viswanathan and P. N. Ponpandian, *Mater. Res. Bull.*, 2017, **95**, 1–8.
25 R. Ghahremanzadeh, Z. Rashid, A. H. Zarnani and H. Naeimi, *RSC Adv.*, 2014, **4**, 43661–43670.
26 D. A. Giannakoudakis, J. K. Mitchell and T. J. Bandosz, *J. Mater. Chem. A*, 2016, **4**, 1008–1019.
27 H. Xia, Y. Wang, J. Lin and L. Lu, *Nanoscale Res. Lett.*, 2011, **6**, 595.
28 S. Ding, S. Chen, D. Luan and Y. Chiang, *Chem. Commun.*, 2011, **47**, 5780–5782.
29 R. Rameshbabu, R. Ramesh, S. Kanagesan, A. Karthigeyan and S. Ponnusamy, *J. Mater. Sci.: Mater. Electron.*, 2014, **25**, 2583–2588.
30 A. Khorsand Zak, W. H. A. Majid, M. E. Abrishami and R. Yousefi, *Solid State Sci.*, 2011, **13**, 251–256.
31 S. E. Shirsath, M. L. Mane, Y. Yasukawa, X. Liu and A. Morisako, *Phys. Chem. Chem. Phys.*, 2014, **16**, 2347–2357.
32 N. A. M. Mokhtar, H. G. Beh and K. C. Lee, *Crystals*, 2019, **9**, 626.
33 W. Wang, Z. Ding, X. Zhao, S. Wu, F. Li, M. Yue and J. P. Liu, *J. Appl. Phys.*, 2015, **117**, 1–5.
34 S. Jovanović, T. Da Ross, A. Ostric, D. Tošić, J. Prekodravac, Z. Marković and B. Todorović Marković, *Phys. Scr.*, 2014, 014023.
35 H. Su, C. Zhang, X. Li, L. Wu and Y. Chen, *RSC Adv.*, 2018, **8**, 39140–39148.
36 K. S. Subrahmanyam, S. R. C. Vivekchand, A. Govindaraj and C. N. R. Rao, *J. Mater. Chem.*, 2008, **18**, 1517–1523.
37 K. Ghosh and S. K. Srivastava, *Dalton Trans.*, 2020, **49**, 16993–17004.
38 B. Wang, P. Guo, H. Bi, Q. Li, G. Zhang, R. Wang, J. Liu, X. S. Zhao, A. Goljanian Tabrizi, N. Arsalani, A. Mohammadi, H. Namazi, L. Saleh Ghadimi, I. Ahadzadeh, K. V. Sankar and R. K. Selvan, *Int. J. Electrochem. Sci.*, 2014, **4**, 4974–4984.
39 L. Mai, H. Li, Y. Zhao, L. Xu, X. Xu, Y. Luo, Z. Zhang, W. Ke, C. Niu and Q. Zhang, *Sci. Rep.*, 2013, **3**, 1–8.
40 L. Q. Mai, F. Yang, Y. L. Zhao, X. Xu, L. Xu and Y. Z. Luo, *Nat. Commun.*, 2011, **2**, 1–5.
41 J. Yan, Z. Fan, W. Sun, G. Ning, T. Wei, Q. Zhang, R. Zhang, L. Zhi and F. Wei, *Adv. Funct. Mater.*, 2012, **22**, 2632–2641.
42 B. Li, M. Zheng, H. Xue and H. Pang, *Inorg. Chem. Front.*, 2016, **3**, 175–202.
43 W. Li, W. Zhang, T. Li, A. Wei, Y. Liu and H. Wang, *Nanoscale Res. Lett.*, 2019, **14**, 229.
44 Y. Wang, Y. Song and Y. Xia, *Chem. Soc. Rev.*, 2016, **45**, 5925–5950.
45 Y. Liu, S. P. Jiang and Z. Shao, *Mater. Today Adv.*, 2020, **7**, 100072.
46 Y. Shao, M. F. El-Kady, J. Sun, Y. Li, Q. Zhang, M. Zhu, H. Wang, B. Dunn and R. B. Kaner, *Chem. Rev.*, 2018, **118**, 9233–9280.
47 J. Shao, X. Zhou, Q. Liu, R. Zou, W. Li, J. Yang and J. Hu, *J. Mater. Chem. A*, 2015, **3**, 6168–6176.
48 Z. H. Huang, T. Y. Liu, Y. Song, Y. Li and X. X. Liu, *Nanoscale*, 2017, **9**, 13119–13127.
49 L. Xu, H. Chen and K. Shu, *J. Sol-Gel Sci. Technol.*, 2016, **77**, 463–469.
50 F. Ding, Z. Yu, X. Chen, X. Chen, C. Chen, Y. Huang, Z. Yang, C. Zou, K. Yang and S. Huang, *Electrochim. Acta*, 2019, **306**, 549–557.
51 A. M. Khattak, H. Yin, Z. A. Ghazi, B. Liang, A. Iqbal, N. A. Khan, Y. Gao, L. Li and Z. Tang, *RSC Adv.*, 2016, **6**, 58994–59000.
52 Y. H. Lee, K. H. Chang and C. C. Hu, *J. Power Sources*, 2013, **227**, 300–308.
53 J. S. Sagu, K. G. U. Wijayantha and A. A. Tahir, *Electrochim. Acta*, 2017, **246**, 870–878.
54 S. N. Khatavkar and S. D. Sartale, *New J. Chem.*, 2020, **44**, 6778–6790.
55 K. V. Sankar and R. K. Selvan, *RSC Adv.*, 2014, **4**, 17555.

56 R. Ramachandran, M. Saranya, C. Santhosh, V. Velmurugan, B. P. C. Raghupathy, S. K. Jeong and A. N. Grace, *RSC Adv.*, 2014, **4**, 21151–21162.
57 A. V. Fulari, M. V. Ramana Reddy, S. T. Jadhav, G. S. Ghodake, D. Y. Kim and G. M. Lohar, *J. Mater. Sci.: Mater. Electron.*, 2018, **29**, 10814–10824.
58 R. S. Ingole, S. B. Kondawar and B. J. Lokhande, *J. Mater. Sci.: Mater. Electron.*, 2017, **28**, 2385–2391.
59 D. C. Papan Xu, K. Ye, M. Du, J. Liu, K. Cheng, J. Yin and G. Wang, *RSC Adv.*, 2015, **5**, 36656–36664.
60 C. Zhao, Y. Jiang, S. Liang, F. Gao, L. Xie and L. Chen, *CrystEngComm*, 2020, **22**, 2953–2963.
61 R. Sahoo, T. H. Lee, D. T. Pham, T. H. T. Luu and Y. H. Lee, *ACS Nano*, 2019, **13**, 10776–10786.
62 G. Singh and S. Chandra, *Int. J. Hydrogen Energy*, 2018, **43**, 4058–4066.
63 P. Guo, Z. Li, S. Liu, J. Xue, G. Wu, H. Li and X. S. Zhao, *J. Mater. Sci.*, 2017, **52**, 5359–5365.
64 L. Li, Z. A. Hu, N. An, Y. Y. Yang, Z. M. Li and H. Y. Wu, *J. Phys. Chem. C*, 2014, **118**, 22865–22872.
65 S. L. Kuo and N. L. Wu, *J. Power Sources*, 2006, **162**, 1437–1443.
66 N. Arsalani, A. G. Tabrizi and L. S. Ghadimi, *J. Mater. Sci.: Mater. Electron.*, 2018, **29**, 6077–6085.
67 W. Cai, T. Lai, W. Dai and J. Ye, *J. Power Sources*, 2014, **255**, 170–178.